

Modified structure of protons and neutrons in correlated pairs

The CLAS Collaboration*

The atomic nucleus is made of protons and neutrons (nucleons), which are themselves composed of quarks and gluons. Understanding how the quark–gluon structure of a nucleon bound in an atomic nucleus is modified by the surrounding nucleons is an outstanding challenge. Although evidence for such modification—known as the EMC effect—was first observed over 35 years ago, there is still no generally accepted explanation for its cause^{1–3}. Recent observations suggest that the EMC effect is related to close-proximity short-range correlated (SRC) nucleon pairs in nuclei^{4,5}. Here we report simultaneous, high-precision measurements of the EMC effect and SRC abundances. We show that EMC data can be explained by a universal modification of the structure of nucleons in neutron–proton SRC pairs and present a data-driven extraction of the corresponding universal modification function. This implies that in heavier nuclei with many more neutrons than protons, each proton is more likely than each neutron to belong to an SRC pair and hence to have distorted quark structure. This universal modification function will be useful for determining the structure of the free neutron and thereby testing quantum chromodynamics symmetry-breaking mechanisms and may help to discriminate between nuclear physics effects and beyond-the-standard-model effects in neutrino experiments.

We study nuclear and nucleon structure by scattering high-energy electrons from nuclear targets. The energy and momentum transferred from the electron to the target determines the space–time resolution of the reaction and thereby which objects are probed (that is, quarks or nucleons). To study the structure of nuclei in terms of individual nucleons, we scatter electrons in quasi-elastic kinematics, where the transferred momentum typically ranges from 1 to 2 GeV c^{-1} and the transferred energy is consistent with elastic scattering from a moving nucleon. To study the structure of nucleons in terms of quarks and gluons, we use deep inelastic scattering (DIS) kinematics, with larger transferred energies and momenta.

Atomic nuclei are broadly described by the nuclear shell model, in which protons and neutrons move in well-defined quantum orbitals, under the influence of an average mean field created by their mutual interactions. The internal quark–gluon substructure of nucleons was originally expected to be independent of the nuclear environment because quark interactions occur at shorter-distance and higher-energy scales than nuclear interactions. However, DIS measurements indicate that quark momentum distributions in nucleons are modified when nucleons are bound in atomic nuclei^{1,2,6,7}, breaking down the scale separation between nucleon structure and nuclear structure.

This scale-separation breakdown in nuclei was first observed thirty-five years ago in DIS measurements performed by the European Muon Collaboration (EMC) at CERN⁸. These showed a decrease of the DIS cross-section ratio of iron to deuterium in a kinematical region corresponding to moderate- to high-momentum quarks in the bound nucleons. The EMC effect has been confirmed by subsequent measurements on a wide variety of nuclei, using both muons and electrons^{9,10}, and over a large range of transferred momenta (see reviews in refs^{1,2,6,7}). The maximum reduction in the DIS cross-section ratio

of a nucleus relative to deuterium increases from about 10% for ⁴He to about 20% for Au.

The EMC effect is now largely accepted as evidence that the momentum distributions of quarks in bound nucleons are different from those of quarks in free nucleons^{1,2,7}. However, there is still no consensus as to the underlying nuclear dynamics that drives it.

Currently, there are two leading approaches for describing the EMC effect, which are both consistent with data: (i) all nucleons are slightly modified when bound in nuclei, or (ii) nucleons are unmodified most of the time, but are modified substantially when they fluctuate into SRC pairs (see ref. ¹ for a recent review).

SRC pairs are temporal fluctuations of two strongly interacting nucleons in close proximity (see, for example, refs^{1,11}). Electron scattering—denoted (e, e')—experiments in quasi-elastic kinematics have shown that SRC pairing shifts nucleons from low-momentum nuclear shell-model states to high-momentum states with momenta greater than the nuclear Fermi momentum. This ‘high-momentum tail’ has a similar shape for all nuclei. The relative abundance of SRC pairs in a nucleus relative to deuterium approximately equals the ratio of their inclusive (e, e') cross-sections (that is, only the scattered electron is reconstructed) in selected quasi-elastic kinematics^{12–15}.

Recent studies^{16–22} of nuclei from ⁴He to Pb showed that SRC nucleons are ‘isophobic’; that is, similar nucleons are much less likely to pair than dissimilar nucleons, leading to many more neutron–proton (np) SRC pairs than neutron–neutron (nn) and proton–proton (pp) pairs. The probability for a neutron to be part of an np SRC pair is observed to be approximately constant for all nuclei, whereas that for a proton increases approximately as N/Z , the ratio of the number of neutrons (N) to the number of protons²² (Z).

The first experimental evidence supporting the SRC-modification hypothesis as an explanation for the EMC effect came from comparing the abundances of SRC pairs in different nuclei with the magnitude of the EMC effect. Not only do both increase from light to heavy nuclei, but there is a robust linear correlation between them^{4,5}. This suggests that the EMC effect might be related to the high-momentum nucleons in nuclei.

The current analysis aims to clarify whether modification of the quark structure of nucleons in close-proximity pairs can explain the observed EMC effect and to study the implications of this effect for the difference between the modification of protons and neutrons in asymmetric nuclei. To this end, we measured both the DIS and quasi-elastic inclusive cross-sections simultaneously for deuterium and heavier nuclei, thereby reducing the uncertainties in the extraction of the EMC effect and SRC scaling factors. We observed that: (1) the EMC effect in all measured nuclei is consistent with being due to the universal modification of the internal structure of nucleons in np SRC pairs, permitting the first data-driven extraction of this universal modification function, (2) the measured per-proton EMC effect and SRC probabilities continue to increase with atomic mass A for all measured nuclei, whereas the per-neutron ones stop increasing at $A \approx 12$, and (3) the EMC–SRC correlation is no longer linear when the EMC data are not corrected for unequal numbers of proton and neutrons.

*A list of authors and their affiliations appears at the end of the paper.

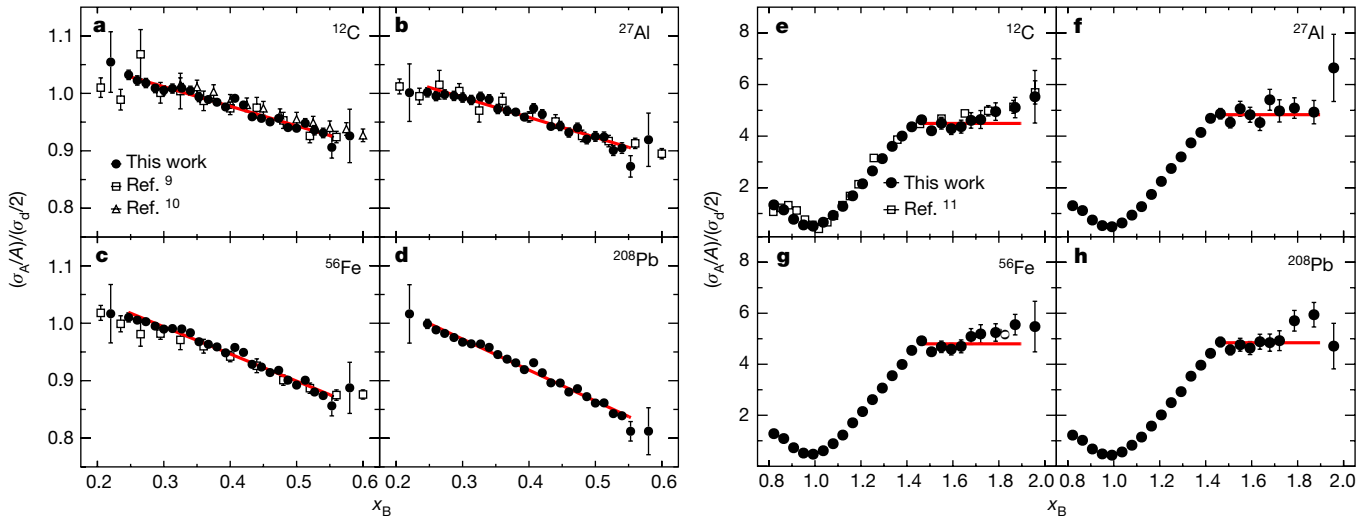


Fig. 1 | DIS and quasi-elastic (e, e') cross-section ratios. **a–d**, Ratio of the per-nucleon electron scattering cross-section of nucleus A ($A = {}^{12}\text{C}$ (**a**), ${}^{27}\text{Al}$ (**b**), ${}^{56}\text{Fe}$ (**c**) and ${}^{208}\text{Pb}$ (**d**)) to that of deuterium for DIS kinematics ($0.2 \leq x_B \leq 0.6$ and $W \geq 1.8$ GeV). The solid points show the data obtained in this work, the open squares show SLAC (Stanford Linear Accelerator Center) data⁹ and the open triangles show Jefferson

Laboratory data¹⁰. The red lines show a linear fit. **e, f**, Corresponding ratios for quasi-elastic kinematics ($0.8 \leq x_B \leq 1.9$). The solid points show the data obtained in this work and the open squares the data of ref. ¹¹. The red lines show a constant fit. The error bars shown include both statistical and point-to-point systematic uncertainties, both at the 1σ or 68% confidence level. The data do not include isoscalar corrections.

We also constrained the internal structure of the free neutron using the extracted universal modification function and we concluded that in neutron-rich nuclei the average proton structure modification will be larger than that of the average neutron.

We analysed experimental data taken using CLAS (CEBAF Large Acceptance Spectrometer)²³ at the Thomas Jefferson National Accelerator Facility (Jefferson Laboratory). In our experiment, a 5.01-GeV electron beam impinged upon a dual target system with a liquid deuterium target cell followed by a foil²⁴ of either C, Al, Fe or Pb. The scattered electrons were detected in CLAS over a wide range of angles and energies, which enabled the extraction of both quasi-elastic and DIS reaction cross-section ratios over a wide kinematical region (see Supplementary Information section I).

The electron scattered from the target by exchanging a single virtual photon with momentum \mathbf{q} and energy ν , giving a four-momentum transfer of $Q^2 = |\mathbf{q}|^2 - \nu^2$. We used these variables to calculate the invariant mass of the nucleon plus virtual photon, $W^2 = (m + \nu)^2 - |\mathbf{q}|^2$ (where m is the nucleon mass), and the Bjorken scaling variable $x_B = Q^2/(2m\nu)$.

We extracted cross-section ratios from the measured event yields by correcting for effects of the experimental conditions, acceptance and momentum reconstruction, as well as reaction effects and bin-centring effects (see Supplementary Information section I). To our knowledge, this was the first precision measurement of inclusive quasi-elastic scattering for SRCs in both Al and Pb, as well as the first measurement of the EMC effect on Pb. For other measured nuclei our data are consistent with previous measurements, but with reduced uncertainties.

The DIS cross-section on a nucleon can be expressed as a function of a single structure function, $F_2(x_B, Q^2)$. In the parton model, x_B represents the fraction of the nucleon momentum carried by the struck quark. $F_2(x_B, Q^2)$ describes the momentum distribution of the quarks in the nucleon, and the ratio $[F_2^A(x_B, Q^2)/A] / [F_2^d(x_B, Q^2)/2]$ describes the relative quark momentum distributions in a nucleus A with mass number A and deuterium^{2,7} (**d**). For brevity, we often omit explicit reference to x_B and Q^2 —that is, we write F_2^A/F_2^d —with the understanding that the structure functions are being compared at identical x_B and Q^2 values. Because the DIS cross-section is proportional to F_2 , experimentally the cross-section ratio of two nuclei is assumed to equal their structure-function ratio^{1,2,6,7}. The magnitude of the EMC effect is defined by the slope of either the cross-section ratios or the structure-function ratios for $0.3 \leq x_B \leq 0.7$ (see Supplementary Information sections IV and V).

Similarly, the relative probability for a nucleon to belong to an SRC pair is interpreted as equal to a_2 , which denotes the average ratio of the inclusive quasi-elastic electron scattering cross-section per nucleon of nucleus A to that of deuterium at momentum transfer^{1,11–15} ($Q^2 > 1.5$ GeV² and $1.45 \leq x_B \leq 1.9$ (see Supplementary Information section III)).

Other nuclear effects are expected to be negligible. The contribution of three-nucleon SRCs should be an order of magnitude smaller than the SRC-pair contributions. The contributions of two-body currents (called ‘higher-twist effects’ in DIS) should also be small (see Supplementary Information section VIII).

Figure 1 shows the DIS and quasi-elastic cross-section ratios for scattering off a solid target relative to deuterium as a function of x_B . The red lines are fits to the data that are used to determine the EMC-effect slopes or SRC scaling coefficients (see Extended Data Tables 1, 2). Typical 1σ cross-section-ratio normalization uncertainties of 1%–2% directly contribute to the uncertainty in the SRC scaling coefficients but introduce negligible uncertainty in the EMC slope. None of the ratios presented has isoscalar corrections (cross-section corrections for unequal numbers of protons and neutrons), in contrast to much published data. We did not apply such corrections for two reasons: (1) to focus on asymmetric nuclei and (2) because isoscalar corrections are model-dependent and differ among experiments^{9,10} (see Extended Data Fig. 1).

The DIS data were cut at $Q^2 > 1.5$ GeV² and $W > 1.8$ GeV, which is just above the resonance region²⁵ and higher than the $W > 1.4$ GeV cut used in previous Jefferson Laboratory measurements¹⁰. The extracted EMC slopes are insensitive to variations in these cuts over Q^2 and W ranges of 1.5–2.5 GeV² and 1.8–2 GeV, respectively (see Supplementary Information Table 7).

Motivated by the correlation between the magnitude of the EMC effect and the SRC-pair density (a_2), we model the modification of the nuclear structure function, F_2^A , as entirely caused by the modification of np SRC pairs. F_2^A is therefore decomposed into contributions from unmodified mean-field protons and neutrons (the first and second terms in equation (1)) and np SRC pairs with modified structure functions (third term):

$$\begin{aligned} F_2^A &= (Z - n_{\text{SRC}}^A) F_2^p + (N - n_{\text{SRC}}^A) F_2^n + n_{\text{SRC}}^A (F_2^{p*} + F_2^{n*}) \\ &= Z F_2^p + N F_2^n + n_{\text{SRC}}^A (\Delta F_2^p + \Delta F_2^n) \end{aligned} \quad (1)$$

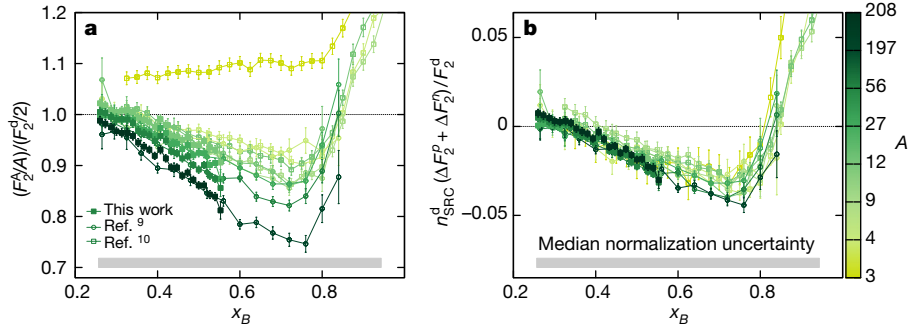


Fig. 2 | Universality of SRC-pair quark distributions. **a, b,** The EMC effect for different nuclei, as observed in ratios of $(F_2^A/A) / (F_2^d/2)$ as a function of x_B (**a**) and the modification of SRC pairs, as described by equation (2) (**b**). Different colours correspond to different nuclei, as indicated by the colour scale on the right. The open circles show SLAC data⁹ and the open squares show Jefferson Laboratory data¹⁰. The nucleus-

where n_{SRC}^A is the number of np SRC pairs in nucleus A , $F_2^p(x_B, Q^2)$ and $F_2^n(x_B, Q^2)$ are the free-proton and free-neutron structure functions, $F_2^{p*}(x_B, Q^2)$ and $F_2^{n*}(x_B, Q^2)$ are the average modified structure functions for protons and neutrons in SRC pairs and $\Delta F_2^n = F_2^{n*} - F_2^n$ (and similarly for ΔF_2^p). F_2^{p*} and F_2^{n*} are assumed to be the same for all nuclei. In this simple model, nucleon-motion effects^{1–3}, which are also dominated by SRC pairs owing to their high relative momentum, are folded into ΔF_2^p and ΔF_2^n .

This model resembles that used in ref. ²⁶. However, that work focused on light nuclei and did not determine the shape of the modification function. Similar ideas using factorization were discussed in ref. ¹, such as a model-dependent ansatz for the modified structure functions, which was shown to be able to describe the EMC data²⁷. The analysis presented here, to our knowledge, is the first data-driven determination of the modified structure functions for nuclei from ³He to Pb.

Because there are no model-independent measurements of F_2^n , we apply equation (1) to the deuteron, rewriting F_2^n as $F_2^d - F_2^p - n_{\text{SRC}}^d (\Delta F_2^p + \Delta F_2^n)$. We then rearrange equation (1) to get:

$$\frac{n_{\text{SRC}}^d (\Delta F_2^p + \Delta F_2^n)}{F_2^d} = \frac{\frac{F_2^A}{F_2^d} - (Z-N) \frac{F_2^p}{F_2^d} - N}{(A/2)a_2 - N} \quad (2)$$

where F_2^p/F_2^d has been previously extracted²⁸ and a_2 is the measured per-nucleon cross-section ratio shown by the red lines in Fig. 1e–h. Here we assume that a_2 approximately equals the per-nucleon SRC-pair density ratio between nucleus A and deuterium^{1,11–15}: $(n_{\text{SRC}}^A/A) / (n_{\text{SRC}}^d/2)$.

Because $\Delta F_2^p + \Delta F_2^n$ is assumed to be nucleus-independent, our model predicts that the left-hand side of equation (2) should be a universal function (that is, the same for all nuclei). This requires that the nucleus-dependent quantities on the right-hand side of equation (2) combine to give a nucleus-independent result.

This is tested in Fig. 2. The left panel shows $[F_2^A(x_B, Q^2)/A] / [F_2^d(x_B, Q^2)/2]$, the per-nucleon structure-function ratio of different nuclei relative to deuterium, without isoscalar corrections. The approximately linear deviation from unity for $0.3 \leq x_B \leq 0.7$ is the EMC effect, which is larger for heavier nuclei. The right panel shows the relative structure modification of nucleons in np SRC pairs, $n_{\text{SRC}}^d (\Delta F_2^p + \Delta F_2^n) / F_2^d$, extracted using the right-hand side of equation (2).

The EMC slope for all measured nuclei increases monotonically with A whereas the slope of the SRC-modified structure function is constant within uncertainties; see Fig. 3 and Extended Data Table 2. Even ³He, which has a markedly different structure-function ratio owing to its very large proton-to-neutron ratio of 2, has a remarkably similar modified structure function to the other nuclei, with the same slope. Thus, we conclude that the magnitude of the EMC effect in different

nuclei can be described by the abundance of np SRC pairs and that the proposed SRC-pair modification function is in fact universal. This universality appears to hold even beyond $x_B = 0.7$.

The universal function extracted here will be tested directly in the future using lattice quantum chromodynamics (QCD) calculations²⁶ and by measuring semi-inclusive DIS off the deuteron, tagged by the detection of a high-momentum backward-recoiling proton or neutron, that will enable direct quantification of the relationship between the momentum and the structure-function modification of bound nucleons²⁹.

The universal SRC-pair modification function can also be used to extract the free neutron-to-proton structure-function ratio, F_2^n/F_2^p , by applying equation (1) to the deuteron and using the measured proton and deuteron structure functions (see Extended Data Fig. 1). In addition to its own importance, this F_2^n can be used to apply self-consistent isoscalar corrections to the EMC effect data (see Supplementary Information equation (5)).

To further test the SRC-driven EMC model, we consider the isophobic nature of SRC pairs (that is, np dominance), which leads to an approximately constant probability for a neutron to belong to an SRC pair in medium-to-heavy nuclei, while the proton probability increases²² as N/Z . If the EMC effect is indeed driven by high-momentum SRCs, then in neutron-rich nuclei both the neutron EMC effect and the SRC probability should saturate, whereas for protons both should grow with nuclear mass and neutron excess. This is done by

independent (universal) behaviour of the SRC modification, as predicted by the SRC-driven EMC model, is clearly observed. The error bars show both statistical and point-to-point systematic uncertainties, both at the 1σ or 68% confidence level, and the grey bands show the median normalization uncertainty at the 1σ or 68% confidence level. The data do not include isoscalar corrections.

independent (universal) behaviour of the SRC modification, as predicted by the SRC-driven EMC model, is clearly observed. The error bars show both statistical and point-to-point systematic uncertainties, both at the 1σ or 68% confidence level, and the grey bands show the median normalization uncertainty at the 1σ or 68% confidence level. The data do not include isoscalar corrections.

independent (universal) behaviour of the SRC modification, as predicted by the SRC-driven EMC model, is clearly observed. The error bars show both statistical and point-to-point systematic uncertainties, both at the 1σ or 68% confidence level, and the grey bands show the median normalization uncertainty at the 1σ or 68% confidence level. The data do not include isoscalar corrections.

independent (universal) behaviour of the SRC modification, as predicted by the SRC-driven EMC model, is clearly observed. The error bars show both statistical and point-to-point systematic uncertainties, both at the 1σ or 68% confidence level, and the grey bands show the median normalization uncertainty at the 1σ or 68% confidence level. The data do not include isoscalar corrections.

independent (universal) behaviour of the SRC modification, as predicted by the SRC-driven EMC model, is clearly observed. The error bars show both statistical and point-to-point systematic uncertainties, both at the 1σ or 68% confidence level, and the grey bands show the median normalization uncertainty at the 1σ or 68% confidence level. The data do not include isoscalar corrections.

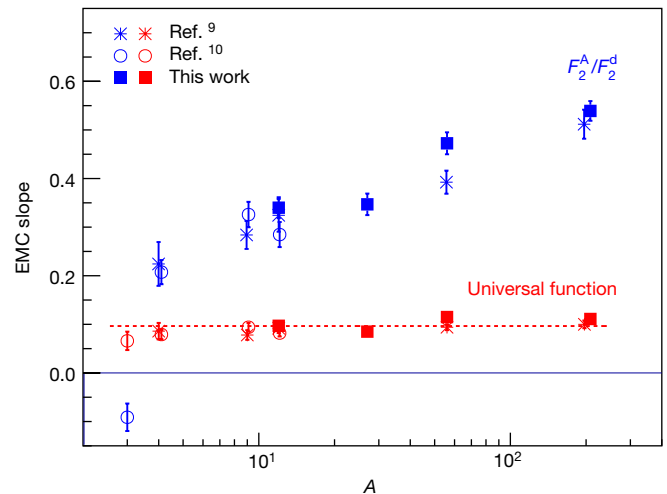


Fig. 3 | EMC and universal modification function slopes. The slopes of the EMC effect for different nuclei from Fig. 2a (blue) and of the universal function from Fig. 2b (red). The error bars shown include the fit uncertainties at the 1σ or 68% confidence level.

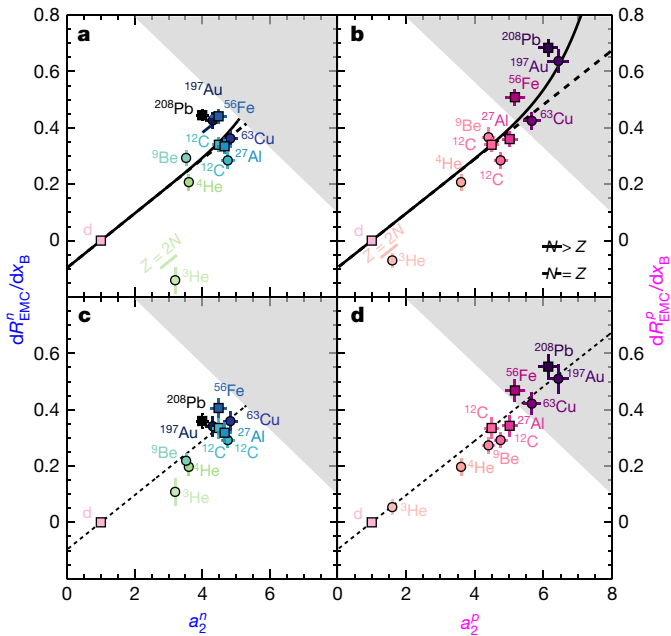


Fig. 4 | Growth and saturation of the EMC effect for protons and neutrons. **a, b,** The per-neutron (**a**) and per-proton (**b**) strength of the EMC effect versus the corresponding per-neutron and per-proton number of SRC pairs. **c, d,** As in **a** and **b**, but with isoscalar corrections. Data obtained in this work are shown by squares and existing data by circles. The dashed lines show the results of equation (1) using the universal modification function shown in Fig. 2 for symmetric ($N = Z$) nuclei. The solid lines show the same results for actual nuclei. The grey regions show the effects of per-neutron saturation. The error bars show both statistical and systematic uncertainties at the 1σ or 68% confidence level.

examining the correlation of the individual per-proton and per-neutron quasi-elastic SRC cross-section ratios, $a_2^p = (\sigma_N/Z) / \sigma_d$ and $a_2^n = (\sigma_N/N) / \sigma_d$, and DIS EMC slopes, dR_{EMC}^p/dx_B and dR_{EMC}^n/dx_B (see Extended Data Tables 1, 3 and Supplementary Information sections III and V).

Figure 4 shows the per-proton and per-neutron EMC slopes as a function of a_2^p and a_2^n , respectively. We consider these correlations both before (Fig. 4a, b) and after (Fig. 4c, d) applying isoscalar corrections to the EMC data and compare them with the predictions of the SRC-driven EMC model. By not applying isoscalar corrections, Fig. 4a, b allows focusing on the separate behaviour of protons and neutrons. Applying self-consistent isoscalar corrections makes both the per-neutron and per-proton EMC–SRC correlations linear, in overall agreement with the model prediction for $N = Z$ nuclei.

This simple rescaling of the previous EMC–SRC correlation result^{4,5}, as expected, does not change the EMC–SRC correlation or its slope. However, the per-neutron and per-proton results differ considerably. Because the probability that a neutron belongs to an SRC pair does not increase for nuclei heavier than C ($A = 12$)²², our model predicts that the per-neutron EMC effect (that is, the slope of $\frac{F_2^N/N}{F_2^d/1}$) will also not increase for $A \geq 12$. By contrast, the probability that a proton belongs to an SRC pair continues to increase for all measured nuclei²² and therefore the per-proton EMC effect should continue to increase. This saturation/no-saturation behaviour is a non-trivial prediction of our model that is supported by the data.

In the per-neutron correlation, the proton-rich ${}^3\text{He}$ point is far below the simple straight line, whereas the neutron-rich Fe and Pb points are above it. In the per-proton correlation, the proton-rich ${}^3\text{He}$ point is below the simple straight line for $N = Z$ nuclei, whereas increasingly neutron-rich heavy nuclei are above it. These features of the data are all well described by our SRC-driven EMC model.

To conclude, the association of the EMC effect with SRC pairs implies that it is a dynamical effect. Most of the time, nucleons bound in nuclei

have the same internal structure as that of free nucleons. However, for short time intervals during which two nucleons form a temporary high-local-density SRC pair, their internal structure is briefly modified. When the two nucleons disassociate, their internal structure again becomes similar to that of free nucleons. This dynamical picture differs markedly from the traditional static modification in the nuclear mean field, which has been previously proposed as an explanation for the EMC effect.

The new universal modification function presented here has implications for our understanding of fundamental aspects of QCD. For example, the study of the ratio of the d quark to the u quark population in a free nucleon as $x_B \rightarrow 1$ offers a stringent test of symmetry-breaking mechanisms in QCD. This can be extracted from measuring the ratio of the free-proton to the free-neutron structure function. However, the lack of a free-neutron target necessitates the use of proton and deuterium DIS data, which requires corrections for the deuteron EMC effect to extract the free neutron. The universal SRC modification function presented here does just that, in a data-driven manner (see Extended Data Fig. 1).

Turning to neutron-rich nuclei, the larger proton EMC effect has several implications. As the proton has two u quarks and one d quark whereas the neutron has two d quarks and one u quark, the larger average modification of the proton's structure implies a larger average modification of the distribution of u quarks in the nucleus compared to d quarks. This will affect DIS charge-changing neutrino interactions, because neutrinos scatter preferentially from d quarks and anti-neutrinos from u quarks. Different modifications to d and u quark distributions will cause a difference in the neutrino and antineutrino cross-sections in asymmetric nuclei, which could be misinterpreted as a sign of physics beyond the standard model or of CP violation. One example of this is the NuTeV experiment³⁰, which extracted an anomalous value of the standard-model Weinberg mixing angle from neutrino–nucleus and antineutrino–nucleus DIS on iron. It was pointed out³⁰ that this anomaly could be due to differences between the proton and the neutron caused by mean-field effects. Our model provides an alternative mechanism. Similarly, the future DUNE experiment will use high-energy neutrino and antineutrino beams incident on the asymmetric nucleus ${}^{40}\text{Ar}$ to look for differences in neutrino and antineutrino oscillations as a possible mechanism for explaining the matter–antimatter asymmetry. They will therefore also need to take the larger proton EMC effect into account to avoid similar anomalies.

Online content

Any methods, additional references, Nature Research reporting summaries, source data, statements of data availability and associated accession codes are available at <https://doi.org/10.1038/s41586-019-0925-9>.

Received: 8 July 2018; Accepted: 18 December 2018;

Published online 20 February 2019.

- Hen, O., Miller, G. A., Piassetzky, E. & Weinstein, L. B. Nucleon–nucleon correlations, short-lived excitations, and the quarks within. *Rev. Mod. Phys.* **89**, 045002 (2017).
- Norton, P. R. The EMC effect. *Rep. Prog. Phys.* **66**, 1253–1297 (2003).
- Frankfurt, L. & Strikman, M. Hard nuclear processes and microscopic nuclear structure. *Phys. Rep.* **160**, 235–427 (1988).
- Weinstein, L. B., Piassetzky, E., Higinbotham, D. W., Gomez, J., Hen, O. & Shneur, R. Short range correlations and the EMC effect. *Phys. Rev. Lett.* **106**, 052301 (2011).
- Hen, O., Piassetzky, E. & Weinstein, L. B. New data strengthen the connection between short range correlations and the EMC effect. *Phys. Rev. C* **85**, 047301 (2012).
- Geesaman, D., Saito, K. & Thomas, A. The nuclear EMC effect. *Annu. Rev. Nucl. Part. Sci.* **45**, 337–390 (1995).
- Malace, S., Gaskell, D., Higinbotham, D. W. & Cloet, I. The challenge of the EMC effect: existing data and future directions. *Int. J. Mod. Phys. E* **23**, 1430013 (2014).
- Aubert, J. et al. The ratio of the nucleon structure functions F_2^N for iron and deuterium. *Phys. Lett. B* **123**, 275–278 (1983).
- Gomez, J. et al. Measurement of the A dependence of deep inelastic electron scattering. *Phys. Rev. D* **49**, 4348–4372 (1994).
- Seely, J. et al. New measurements of the European Muon Collaboration effect in very light nuclei. *Phys. Rev. Lett.* **103**, 202301 (2009).

11. degli Atti, C. C. In-medium short-range dynamics of nucleons: recent theoretical and experimental advances. *Phys. Rep.* **590**, 1–85 (2015).
12. Fomin, N. et al. New measurements of high-momentum nucleons and short-range structures in nuclei. *Phys. Rev. Lett.* **108**, 092502 (2012).
13. Frankfurt, L. L., Strikman, M. I., Day, D. B. & Sargsyan, M. Evidence for short-range correlations from high Q^2 (e,e') reactions. *Phys. Rev. C* **48**, 2451–2461 (1993).
14. CLAS Collaboration. Observation of nuclear scaling in the $A(e,e')$ reaction at $x_B > 1$. *Phys. Rev. C* **68**, 014313 (2003).
15. CLAS Collaboration. Measurement of two- and three-nucleon short-range correlation probabilities in nuclei. *Phys. Rev. Lett.* **96**, 082501 (2006).
16. Tang, A. et al. n - p short-range correlations from $(p, 2p + n)$ measurements. *Phys. Rev. Lett.* **90**, 042301 (2003).
17. Piasetzky, E., Sargsian, M., Frankfurt, L., Strikman, M. & Watson, J. W. Evidence for strong dominance of proton–neutron correlations in nuclei. *Phys. Rev. Lett.* **97**, 162504 (2006).
18. Shneor, R. et al. Investigation of proton–proton short-range correlations via the $^{12}\text{C}(e,e'pp)$ reaction. *Phys. Rev. Lett.* **99**, 072501 (2007).
19. Subedi, R. et al. Probing cold dense nuclear matter. *Science* **320**, 1476–1478 (2008).
20. Korover, I. et al. Probing the repulsive core of the nucleon–nucleon interaction via the $^4\text{He}(e,e'pN)$ triple-coincidence reaction. *Phys. Rev. Lett.* **113**, 022501 (2014).
21. CLAS Collaboration. Momentum sharing in imbalanced Fermi systems. *Science* **346**, 614–617 (2014).
22. CLAS Collaboration. Probing high-momentum protons and neutrons in neutron-rich nuclei. *Nature* **560**, 617 (2018).
23. Mecking, B. A. et al. The CEBAF large acceptance spectrometer (CLAS). *Nucl. Instrum. Meth. A* **503**, 513–553 (2003).
24. Hakobyan, H. et al. A double target system for precision measurements of nuclear medium effects. *Nucl. Instrum. Meth. A* **592**, 218–223 (2008).
25. CLAS Collaboration. Measurement of the neutron F_2 structure function via spectator tagging with CLAS. *Phys. Rev. Lett.* **108**, 142001 (2012); erratum **108**, 199902 (2012).
26. Chen, J.-W., Detmold, W., Lynn, J. E. & Schwenk, A. Short-range correlations and the EMC effect in effective field theory. *Phys. Rev. Lett.* **119**, 262502 (2017).
27. Hen, O., Higinbotham, D. W., Miller, G. A., Piasetzky, E. & Weinstein, L. B. The EMC effect and high momentum nucleons in nuclei. *Int. J. Mod. Phys. E* **22**, 1330017 (2013).
28. Arrington, J., Coester, F., Holt, R. J. & Lee, T. S. H. Neutron structure functions. *J. Phys. G* **36**, 025005 (2009).
29. Hen, O. et al. In medium nucleon structure functions, SRC, and the EMC effect. Preprint at <https://arxiv.org/abs/1409.1717> (2014).
30. Cloët, I. C., Bentz, W. & A. W. Thomas, A. W. Isovector EMC effect explains the NuTeV anomaly. *Phys. Rev. Lett.* **102**, 252301 (2009).

Acknowledgements We acknowledge the efforts of the staff of the Accelerator and Physics divisions at Jefferson Laboratory that made this experiment possible. The analysis presented here was carried out as part of the Jefferson Laboratory Hall B Data-Mining project, supported by the US Department of Energy (DOE). The research was also supported by the National Science Foundation, the Israel Science Foundation, the Chilean Comisión Nacional de Investigación Científica y Tecnológica, the French Centre National de la Recherche Scientifique and Commissariat à l’Énergie Atomique, the French–American Cultural Exchange, the Italian Istituto Nazionale di Fisica Nucleare, the National Research Foundation of Korea and the UK Science and Technology Facilities Council. The research of M.S. was supported by the US DOE, Office of Science, Office of Nuclear Physics, under award number DE-FG02-93ER40771. Jefferson Science Associates operates the Thomas Jefferson National Accelerator Facility for the DOE, Office of Science, Office of Nuclear Physics under contract DE-AC05-06OR23177.

Author contributions CLAS was designed and constructed by the CLAS Collaboration and Jefferson Laboratory. Data acquisition, processing and calibration, Monte Carlo simulations of the detector and data analyses were performed by a large number of CLAS Collaboration members, who also discussed and approved the scientific results. The analysis presented here was performed by B.S. and A.S. with input from S.G., O.H., E. Piasetzky and L.B.W. and reviewed by the CLAS collaboration.

Competing interests The authors declare no competing interests.

Additional information

Extended data is available for this paper at <https://doi.org/10.1038/s41586-019-0925-9>.

Supplementary information is available for this paper at <https://doi.org/10.1038/s41586-019-0925-9>.

Reprints and permissions information is available at <http://www.nature.com/reprints>.

Publisher’s note: Springer Nature remains neutral with regard to jurisdictional claims in published maps and institutional affiliations.

© The Author(s), under exclusive licence to Springer Nature Limited 2019

The CLAS Collaboration

B. Schmookler¹, M. Duer², A. Schmidt¹, O. Hen^{1*}, S. Gilad¹, E. Piasetzky², M. Strikman³, L. B. Weinstein⁴, S. Adhikari⁵, M. Amarian⁴, A. Ashkenazi¹, H. Avakian⁶, J. Ball⁷, I. Balossino⁸, L. Barion⁸, M. Bashkanov⁹, M. Battaglieri¹⁰, A. Beck¹, I. Bedlinskiy¹¹, A. S. Biselli¹², S. Boiarinov⁶, W. J. Briscoe¹³, W. K. Brooks^{6,14}, V. D. Burkert⁶, D. S. Carman⁶, A. Celentano¹⁰, R. G. Charles⁴, T. Chetry¹⁵, G. Ciullo^{8,16}, E. Cohen², P. L. Cole¹⁷, V. Crede¹⁸, R. Cruz-Torres¹, A. D’Angelo^{19,20}, N. Dashyan²¹, E. De Sanctis²², R. De Vita¹⁰, A. Deur⁶, S. Diehl²³, C. Djalali¹⁵, R. Dupre²⁴, H. Egiyan⁶, L. El Fassi²⁵, L. Elouadrhiri⁶, P. Eugenio¹⁸, G. Fedotov¹⁵, R. Fersch^{26,27}, A. Filippi²⁸, T. A. Forest²⁹, G. Gavalian⁶, G. P. Gilfoyle³⁰, F. X. Girod⁶, E. Golovatch³¹, R. W. Gothe³², K. A. Griffioen²⁷, M. Guidal²⁴, L. Guo^{5,6}, K. Hafidi³³, H. Hakobyan^{14,21}, C. Hanretty⁶, N. Harrison⁶, F. Hauenstein⁴, T. B. Hayward²⁷, K. Hicks¹⁵, D. Higinbotham⁶, M. Holtrop³⁴, C. E. Hyde⁴, Y. Ilieva^{13,32}, D. G. Ireland³⁵, B. S. Ishkhanov³¹, E. L. Isupov³¹, H.-S. Jo³⁶, S. Johnston³³, K. Joo²³, S. Joosten³³, M. L. Kabir²⁵, D. Keller³⁷, G. Khachatryan²¹, M. Khachatryan⁴, M. Khandaker³⁸, A. Kim²³, W. Kim³⁶, A. Klein⁴, F. J. Klein³⁹, I. Korover⁴⁰, V. Kubarovskiy⁶, S. E. Kuhn⁶, S. V. Kuleshov^{11,14}, L. Lanza¹⁹, G. Laskaris¹, P. Lenisa⁸, K. Livingston³⁵, I. J. D. MacGregor³⁵, N. Markov²³, B. McKinnon³⁵, S. Mey-Tal Beck¹, T. Mineeva¹⁴, M. Mirazita²², V. Moiseev^{6,31}, R. A. Montgomery³⁵, C. Munoz Camacho²⁴, B. Mustapha³³, S. Nicolai²⁴, M. Osipenko¹⁰, A. I. Ostrovidov¹⁸, M. Paolone⁴¹, R. Paremuzyan³⁴, K. Park^{6,36}, E. Pasyuk^{6,42}, M. Patsyuk¹, O. Pogorelko¹¹, J. W. Price⁴³, Y. Prok^{4,37}, D. Protopopescu³⁵, M. Ripani¹⁰, D. Riser²³, A. Rizzo^{19,20}, G. Rosner³⁵, P. Rossi^{6,22}, F. Sabatié⁷, C. Salgado³⁸, R. A. Schumacher⁴⁴, E. P. Segarra¹, Y. G. Sharabian⁶, I. U. Skorodumina^{31,32}, D. Sokhan³⁵, N. Sparveris⁴¹, S. Stepanyan⁶, S. Strauch^{13,32}, M. Taiuti^{10,45}, J. A. Tan³⁶, M. Ungaro^{6,46}, H. Voskanyan²¹, E. Voutier²⁴, D. P. Watts⁹, X. Wei⁶, M. Wood⁴⁷, N. Zachariou⁹, J. Zhang³⁷, Z. W. Zhao^{4,48} & X. Zheng³⁷

¹Massachusetts Institute of Technology, Cambridge, MA, USA. ²Tel Aviv University, Tel Aviv, Israel. ³Pennsylvania State University, University Park, PA, USA. ⁴Old Dominion University, Norfolk, VA, USA. ⁵Florida International University, Miami, FL, USA. ⁶Thomas Jefferson National Accelerator Facility, Newport News, VA, USA. ⁷IRFU, CEA, Université Paris-Saclay, Gif-sur-Yvette, France. ⁸INFN, Sezione di Ferrara, Ferrara, Italy. ⁹University of York, Heslington, UK. ¹⁰INFN, Sezione di Genova, Genoa, Italy. ¹¹Institute of Theoretical and Experimental Physics, Moscow, Russia. ¹²Fairfield University, Fairfield, CT, USA. ¹³The George Washington University, Washington, DC, USA. ¹⁴Universidad Técnica Federico Santa María, Valparaíso, Chile. ¹⁵Ohio University, Athens, OH, USA. ¹⁶Università di Ferrara, Ferrara, Italy. ¹⁷Lamar University, Beaumont, TX, USA. ¹⁸Florida State University, Tallahassee, FL, USA. ¹⁹INFN, Sezione di Roma Tor Vergata, Rome, Italy. ²⁰Università di Roma Tor Vergata, Rome, Italy. ²¹Yerevan Physics Institute, Yerevan, Armenia. ²²INFN, Laboratori Nazionali di Frascati, Frascati, Italy. ²³University of Connecticut, Storrs, CT, USA. ²⁴Institut de Physique Nucléaire, CNRS/IN2P3, Université Paris-Sud, Université Paris-Saclay, Orsay, France. ²⁵Mississippi State University, Mississippi State, MS, USA. ²⁶Christopher Newport University, Newport News, VA, USA. ²⁷College of William and Mary, Williamsburg, VA, USA. ²⁸INFN, Sezione di Torino, Turin, Italy. ²⁹Idaho State University, Pocatello, ID, USA. ³⁰University of Richmond, Richmond, VA, USA. ³¹Skobeltsyn Institute of Nuclear Physics, Lomonosov Moscow State University, Moscow, Russia. ³²University of South Carolina, Columbia, SC, USA. ³³Argonne National Laboratory, Argonne, IL, USA. ³⁴University of New Hampshire, Durham, NH, USA. ³⁵University of Glasgow, Glasgow, UK. ³⁶Kyungpook National University, Daegu, Korea. ³⁷University of Virginia, Charlottesville, VA, USA. ³⁸Norfolk State University, Norfolk, VA, USA. ³⁹Catholic University of America, Washington, DC, USA. ⁴⁰Nuclear Research Centre Negev, Beer-Sheva, Israel. ⁴¹Temple University, Philadelphia, PA, USA. ⁴²Arizona State University, Tempe, AZ, USA. ⁴³California State University, Carson, CA, USA. ⁴⁴Carnegie Mellon University, Pittsburgh, PA, USA. ⁴⁵Università di Genova, Dipartimento di Fisica, Genoa, Italy. ⁴⁶Rensselaer Polytechnic Institute, Troy, NY, USA. ⁴⁷Canisius College, Buffalo, NY, USA. ⁴⁸Duke University, Durham, NC, USA. *e-mail: hen@mit.edu

METHODS

Experimental setup and electron identification. CLAS used a toroidal magnetic field with six sectors of drift chambers, scintillation counters, Cerenkov counters and electromagnetic calorimeters to identify electrons and reconstruct their trajectories²³. The experiment used a specially designed double-target setup, consisting of a solid target and a 2-cm long cryo-target cell containing liquid deuterium²⁴. The cryo-target cell and solid target were separated by 4 cm, with a thin isolation foil between them. Both targets and the isolation foil were kept in the beamline simultaneously; this allowed an accurate measurement of cross-section ratios of nuclei relative to deuterium. A dedicated control system was used to position one of six different solid targets (thin and thick Al, Sn, C, Fe and Pb, all at natural abundance) at a time during the experiment. The main data collected during the experiment were for a target configuration of deuterium plus C, Fe or Pb and for an empty cryo-target cell with the thick Al target. We identified electrons by requiring that the track originating in the liquid deuterium or solid targets produced a large enough signal in the Cerenkov counter and deposited enough energy in the electromagnetic calorimeter (see refs^{21,22} for details).

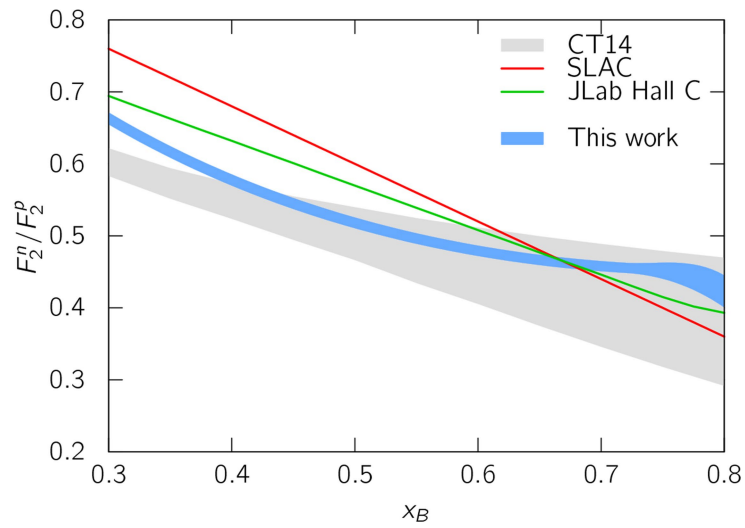
Vertex reconstruction. Electrons scattering from the solid and cryo-targets were selected using vertex cuts with a resolution of several millimetres (depending on the scattering angle), which is sufficient to separate the targets, which were 4 cm apart²¹. We considered events with a reconstructed electron vertex up to 0.5 cm outside the 2-cm-long cryo-target to originate from the deuterium. Similarly, for the solid target we considered events with a reconstructed electron vertex up to 1.5 cm around it.

Background subtraction. There were two main sources of background in the measurement: (1) electrons scattering from the Al walls of the cryo-target cell, and (2) electrons scattering from the isolation foil between the cryo-target and the solid target. When the vertex of these electrons was reconstructed within the region of the deuterium target, they falsely contributed to the cross-section associated with the deuterium target. Data from measurements using an empty cryo-target were used to subtract these contributions. In the case of quasi-elastic scattering, at $x_B > 1$, these measurements did not have sufficient statistics to allow a reliable background subtraction. We therefore required quasi-elastic deuterium electrons to be reconstructed in the inner 1 cm of the 2-cm-long cryo-target. This increased the reliability of the background subtraction but reduced the deuterium statistics by a factor of two. Data from runs with a full cryo-target and no solid target were used to subtract background from electron scattering events with a reconstructed vertex in the solid-target region, originating from the isolation foil or the cryo-target.

To increase statistics, the analysis combined all deuterium data, regardless of the solid target placed with the deuterium in the beamline. We considered only runs in which the electron scattering rate from the cryo-target deviated by less than 4% from the average. The systematic uncertainties associated with the vertex cuts, target-wall subtraction and combination of deuterium data from different runs are described in Supplementary Information section 2.

Data availability

The raw data from this experiment are archived in Jefferson Laboratory's mass storage silo.



Extended Data Fig. 1 | models. F_2^n/F_2^p Ratio of neutron to proton structure functions, F_2^n/F_2^p , derived from the SRC-driven EMC model (blue band) used in the isoscalar corrections of refs ⁹ (SLAC, red line) and ¹⁰ (JLab Hall C; green line) and derived in the CTEQ-14 global fit, shown

here for $Q^2 = 10 \text{ GeV}^2$ (grey band). The large spread among the various models shows the uncertainty in F_2^n , a key ingredient in the isoscalar corrections previously applied to the EMC effect data.

Extended Data Table 1 | SRC scaling coefficients

Nucleus	This work			Ref. [5]		
	a_2	a_2^p	a_2^n	a_2	a_2^p	a_2^n
^3He				2.13 ± 0.04	1.60 ± 0.03	3.20 ± 0.06
^4He				3.60 ± 0.10	3.60 ± 0.10	3.60 ± 0.10
^9Be				3.91 ± 0.12	4.40 ± 0.14	3.52 ± 0.11
^{12}C	4.49 ± 0.17	4.49 ± 0.17	4.49 ± 0.17	4.75 ± 0.16	4.75 ± 0.16	4.75 ± 0.16
^{27}Al	4.83 ± 0.18	5.02 ± 0.19	4.66 ± 0.17			
^{56}Fe	4.80 ± 0.22	5.17 ± 0.24	4.48 ± 0.21			
^{63}Cu				5.21 ± 0.20	5.66 ± 0.22	4.83 ± 0.19
^{197}Au				5.16 ± 0.22	6.43 ± 0.27	4.31 ± 0.18
^{208}Pb	4.84 ± 0.20	6.14 ± 0.25	3.99 ± 0.17			

Per-nucleon (a_2), per-proton (a_2^p) and per-neutron (a_2^n) SRC scale factors for different nuclei relative to deuterium. The 1σ or 68% confidence level uncertainties shown include the fit uncertainties.

Extended Data Table 2 | EMC slopes

Nucleus	dR_{EMC}/dx_B			Universal Function Slope		
	JLab Hall C	SLAC	This Work	JLab Hall C	SLAC	This Work
^3He	0.091±0.028			-0.066±0.019		
^4He	-0.207±0.025	-0.222±0.045		-0.080±0.010	-0.086±0.017	
^9Be	-0.326±0.026	-0.283±0.028		-0.094±0.009	-0.078±0.010	
^{12}C	-0.285±0.026	-0.322±0.033	-0.340±0.022	-0.082±0.007	-0.092±0.010	-0.097±0.006
^{27}Al			-0.347±0.022			-0.086±0.006
^{56}Fe		-0.391±0.025	-0.472±0.023		-0.094±0.006	-0.115±0.006
^{63}Cu		-0.391±0.025			-0.094±0.006	
^{197}Au		-0.511±0.030			-0.100±0.008	
^{208}Pb			-0.539±0.020			-0.111±0.005

Slopes of non-isoscalar-corrected F_2^A/F_2^d (dR_{EMC}/dx_B) and of the universal function, shown in Fig. 2a, b. The SLAC data are from ref. ⁹ and the Jefferson Laboratory ('JLab Hall C') data are from ref. ¹⁰. The slopes are obtained from a linear fit of the data for $0.25 \leq x_B \leq 0.7$. The 1 σ or 68% confidence level uncertainties shown include the fit uncertainties.

Extended Data Table 3 | Per nucleon, per-proton and per-neutron EMC slopes

Nucleus	This work			Previous Data		
	dR_{EMC}/dx_B	dR_{EMC}^p/dx_B	dR_{EMC}^n/dx_B	dR_{EMC}/dx_B	dR_{EMC}^p/dx_B	dR_{EMC}^n/dx_B
^3He				0.091 ± 0.028	0.068 ± 0.021	0.137 ± 0.041
^4He				-0.207 ± 0.025	-0.207 ± 0.025	-0.207 ± 0.025
^9Be				-0.326 ± 0.026	-0.367 ± 0.029	-0.293 ± 0.024
^{12}C	-0.340 ± 0.022	-0.340 ± 0.022	-0.340 ± 0.022	-0.285 ± 0.026	-0.285 ± 0.026	-0.285 ± 0.026
^{27}Al	-0.347 ± 0.022	-0.360 ± 0.023	-0.335 ± 0.021			
^{56}Fe	-0.472 ± 0.023	-0.509 ± 0.024	-0.441 ± 0.021	-0.391 ± 0.025	-0.421 ± 0.027	-0.365 ± 0.023
^{63}Cu				-0.391 ± 0.025	-0.425 ± 0.027	-0.362 ± 0.023
^{197}Au				-0.511 ± 0.030	-0.637 ± 0.037	-0.427 ± 0.025
^{208}Pb	-0.539 ± 0.020	-0.684 ± 0.026	-0.445 ± 0.017			

Per-nucleon (dR_{EMC}/dx_B), per-proton (dR_{EMC}^p/dx_B) and per-neutron (dR_{EMC}^n/dx_B) EMC slopes from the current and previous studies used in Fig. 4. The previous data include Jefferson Laboratory ('JLab Hall C') results¹⁰ for light nuclei ($A \leq 12$) and SLAC results⁹ for heavier nuclei. The 1σ or 68% confidence level uncertainties shown include the fit uncertainties.